

Department of Advanced Materials Science

Graduate School of Frontier Sciences

The University of Tokyo

2018

Master's Thesis

Study on the Spin Conversion Induced by
Surface Acoustic Waves

表面弾性波により誘起されたスピン変換現象
に関する研究

Submitted July 17, 2018

Adviser: Professor Yoshichika Otani 印

Mingran Xu

I would like to dedicate this thesis to my loving parents:

许文坛，陈巧云

and sisters:

许冰冰，许荣荣

and life mentor:

吴宣怜

Acknowledgements

It has been an unforgettable journey working on this thesis. It would not have been possible without the help from numerous friends and colleagues.

First of all, I would like to thank Prof.Otani for giving me the opportunity to pursue a Master's degree in his group. Apart from the scientific discussion, I appreciate his thoughtful suggestions and continuous support in all aspects. Besides, I want to thank Prof.Lippmaa for the inspiring discussion and ideas.

I would like to thank all the members in the Quantum Nano-Scale Magnetism Team and Otani Laboratory. Primarily, I would like to thank my excellent advisor Jorge Luis Puebla Nunez and incomparable mentor Florent Auvray for all the scientific and non-scientific helps. It was a pleasant experience working with you as a team that I will never forget. Also, I would like to thank Kondou san, Bivas Rana, Prasanta Kumar Muduli, Kim san, Hanshen Tsai, Matsumoto san and Kim heeman for generously sharing your broad knowledge. I have learned a lot from you.

Special thanks go to the ladies in our group. I would like to thank Ishinabe san, Kaneda san and Ota san for patiently taking care of my document works. Also, I would like to thank Kaito san for the selfless guidance in the device fabrication and in learning Japanese. Besides, I am grateful to Naemi Leo for generously sharing her thesis templates and leading me into a world with Latex and Python.

Many thanks to Emergent Matter Science Research Support Team and Materials Characterization Support Unit for all the technical support. In particular, I want to acknowledge Akimoto san, Hashizume san, Amaya san, Taguchi san and Shihoyama san for the detailed instructions and kind help during device fabrication process.

Moreover, finally, I would like to express my gratitude to all my family members and friends for the perpetual support and love. Thank you so much!♥

Abstract

Since last century, spin conversion, the critical concept of Spintronics, has been vigorously investigated in order to gain a deeper understanding of spin dynamics and enriching the functionalities of electronic devices. It describes various intriguing phenomena taking place at nanoscale between electricity, light, sound, vibration, heat, etc., based on the interconversions mediated by spin. However, among the above, the interaction between spin and sound-vibration prevails not well explored.

This thesis focuses on revealing the mysterious relation between lattice vibrations and spins via magnon-phonon coupling and inverse Edelstein effect at the hybrid devices Ni/Cu(Ag)/Bi₂O₃. By passing surface acoustic waves (SAWs) across magnetoelastic material layers, periodic elastic deformation induced by SAWs drives acoustic ferromagnetic resonance (A-FMR), generating spin current flow into adjacent nonmagnetic layers. With the presence of Rashba spin-orbit coupling at the interface between non-magnetic metal and Bi₂O₃, spin currents transform to electric signals.

The success of the present study brings new insights towards future Spintronics devices. First of all, the generation of spin current ($J_s \approx 1.6 \times 10^8 \text{ A/m}^2$) due to magnon-phonon coupling reveals the viability of acoustic spin pumping as a mechanism for the development of Spintronics devices. Also, the full in-plane magnetic field angle dependence of the power absorption and a combination of longitudinal and transverse voltage detection reveals the symmetric and asymmetric components of the inverse Edelstein effect voltage induced by Rayleigh-type surface acoustic waves. These unique anisotropic responses give new insights toward selectively controlling different types of acoustic phonons by Spintronics devices.

The magnon-phonon coupling is not the only route for transferring mechanical oscillation to spin. In the future, I will focus our study on the direct coupling between spin and mechanical angular momentum (spin-rotation coupling, SRC) by using optical characterization method. The success will bring us the original new method for spin current generation, advancing the understanding of spin conversion phenomena.

Table of contents

List of figures	xi
List of tables	xiii
Introduction	xv
1 Acoustic ferromagnetic resonance	1
1.1 Surface acoustic wave generation	2
1.2 Magnetoelastic magnetization dynamics	4
1.3 Device fabrication process	7
1.3.1 IDTs patterning by using Electron beam lithography	8
1.3.2 X-ray crystallography	11
1.3.3 Experimental setup	11
1.4 Experimental results and discussion	12
1.5 Conclusions and outlook	16
2 Spin to charge conversion induced by magnon-phonon coupling	17
2.1 Rashba splitting	18
2.2 Inverse Edelstein effect	19
2.3 Experimental results and discussion	21
2.3.1 Inverse Edelstein effect voltage detected in transverse and longitudinal geometries	22
2.3.2 Description of fitting formula for IEE voltage detection	25
2.3.3 Angular variation of spin currents generated by acoustic ferro- magnetic resonance	26
2.3.4 Anisotropic distribution of charge potential	27
2.4 Conclusions and outlook	30

3	Conclusions and future perspectives	31
3.1	Conclusions	31
3.2	Future perspectives	32
3.2.1	Spin rotation coupling via surface acoustic waves	32
3.2.2	Numerical simulation results	33
3.2.3	Expected outcome	34
	References	37

List of figures

1.1	Schematic of direct piezoelectric effect (a), reverse piezoelectric effect (b), and an integral device allowing both direct and reverse effects to take place (c).	3
1.2	Acoustic spin pumping (ASP) mechanism acting in a trilayer formed by Ni/Cu/Bi ₂ O ₃	6
1.3	Top view of device layout. IDT1 and IDT2 are designed for investigating the absorption spectrum of SAW while center FM layer is for the interaction of phonon and magnon.	7
1.4	CAD design of sample. Layout of sample	8
1.5	A example of IDTs design in CAD	10
1.6	Scanning electron microscope image(SEM) of fabricated interdigital transducers. (a) and (b) correspond to the devices with center-to-center spacing 400nm and 800nm respectively.	10
1.7	XRD spectroscopy characterization at 0.45° incidence angle. The blue line and red line are the results for Cu/Bi ₂ O ₃ and Ag/Bi ₂ O ₃ , respectively. The same broad peak 28° shown in both blue and red line are characteristic peaks of amorphous Bi ₂ O ₃ . Moreover, the next two peaks, 38.3° in the red line, 43.6° in the blue line, represent the characteristic peak of Ag (111) and Cu (111), respectively.	11
1.8	Illustration of experiment setup. The surface acoustic waves are generated by applying RF voltage on interdigital transducers and the longitudinal voltage and transverse voltage are measured while applying an external magnetic field \mathbf{H} at an angle θ	12
1.9	An example of transmission spectrum measured with (Blue line) and without (Red line) time gating method. Note that this one does not corresponding to the device used in section 1.3	13
1.10	AFMR spectrum	13

1.11	Polar graph of damping of SAW due to acoustically excited FMR measured on (a): Ni/Cu/Bi ₂ O ₃ and (b): Ni/Ag/Bi ₂ O ₃ , varying applied magnetic field angle θ	15
2.1	Schematics of direct Edelstein effect (a), and inverse Edelstein effect (b).	20
2.2	Illustration of experiment setup. The surface acoustic waves are generated by applying RF voltage on interdigital transducers and the longitudinal voltage and transverse voltage are measured while applying an external magnetic field \mathbf{H} at an angle θ	22
2.3	Longitudinal signal measured on Ni/Cu/Bi ₂ O ₃ (red circles) and Ni/Ag/Bi ₂ O ₃ (blue triangles) devices depending on the magnetic field amplitude at $\theta = 240^\circ$. The opposite sign of the signal reflects the opposite configuration of spin text at the Fermi contour	23
2.4	Polar graph of transverse signal measured on (a): Ni/Cu/Bi ₂ O ₃ and (b): Ni/Ag/Bi ₂ O ₃ , varying applied external magnetic field angle θ . Polar graph of longitudinal signal measured on (c): Ni/Cu/Bi ₂ O ₃ and (d): Ni/Ag/Bi ₂ O ₃ , varying applied external magnetic field angle θ	25
2.5	Angular variation of spin current density in (a) Ni/Cu/Bi ₂ O ₃ and (b) Ni/Ag/Bi ₂ O ₃	27
2.6	(a, b) Schematic of measurement configuration 1 and configuration 2, and anisotropic distribution of charge potential; (c, d) Angular variation of transverse voltage measured with configuration 1 and configuration 2.	29
3.1	Schematics of optical characterization on spin rotation coupling . . .	33
3.2	Screenshot of simulation model in COMSOL-Multiphysics	34

List of tables

1.1	Resist preparation	9
1.2	Development	11
3.1	Numerical simulation results	34

Introduction

In recent decades, a new sub-discipline of solid state physics, Spintronics, has been emerging dramatically. Compared with conventional electronics devices, Spintronics devices promise tremendous advantages, such as less heat generation, low power consumption, and higher compatibility. These novel features attract worldwide interest towards this topic. For instance, giant magnetoresistance (GMR) effect has well applied to the high-density storage device in everyone's hard disk. Also, the booming market of magnetoresistive random-access memory (MRAM) has been predicted to dominate the whole memory market shortly. In term of the research towards generation, manipulation and detection of spin polarization, have been continuously making exciting progress. Especially, after embedded with low-dimensional materials, Spintronics again gives a significant impact on physics society, changing the fundamental new view of matters.

The critical concept of Spintronics, spin conversion, lies on generation, manipulation, and detection of spin polarization, which is based on various phenomena taking place at nanoscale between electricity, light, sound, vibration, heat, etc.,[1]. However, despite the continuous progress in the understanding of spin conversion, few studies have systematically demonstrated the interaction between spin and sound-vibration prevails not well explored.

Since the discovery of the Barnett effect, there is a continuous interest in research towards revealing the mysterious relation between mechanical angular momentum and spin. In the presence of magnetic materials, mechanical oscillation can be transferred to spin via the magnon-phonon coupling. By passing surface acoustic waves (SAWs) across ferromagnetic layers, periodic elastic deformation induced by SAWs drives precession magnetization dynamics such as ferromagnetic resonance (FMR), generating spin current flow into adjacent nonmagnetic layers. This process is also known as acoustic spin pumping. After an exciting spin current through magnon-phonon coupling in the presence of spin-orbit coupling (SOC), the spin information translates to electronic information. Efficient conversion via inverse

spin Hall effect (ISHE) or inverse Edelstein effect (IEE) allows accurate analysis of the generated spin current by electrical measurement for characterizing the coupling between magnon and phonon. In ref [2], I demonstrated the feasibility of combining acoustic spin pumping via magnon - phonon coupling and spin to charge conversion via IEE. Full in-plane magnetic field angle dependence of power absorption and the combination of longitudinal and transverse voltage detection reveals symmetric and asymmetric components of acoustic spin pumping voltage induced by Rayleigh-type surface acoustic waves. The generation of spin current ($J_s \approx 1.6 \times 10^8 A/m^2$) through the magnon -phonon coupling reveals the viability of acoustic spin pumping as a mechanism for the development of Spintronic devices. Also, the asymmetric feature of the signal shows new directions of combining Spintronics and SAWs technology.

In the absence of magnetic materials, spin-rotation coupling brings new possibilities of spin current generation via mechanical excitation, free of magnetic fields and spin-orbit interaction. When SAWs couples with nonmagnetic materials like Cu, Ag, etc., it rearranges spin states in the materials, inducing non-equilibrium spin accumulation. To obtain preliminary information, I performed numerical simulation using Comsol-multiphysics software, quantifying the magnitude of spin current in Cu, Al, Ag, GaAs. According to the simulation result, among the candidates, Cu gives the best performance in producing spin current ($J_s = 1.6 \times 10^7 A/m^2$). To avoid the various spurious signals accompanying with SAWs, I propose optical characterization (Magneto-Optical Kerr Effect, MOKE) as an unambiguous detection method to elucidate the spin rotation coupling in solids. As a first step towards this direction, our group succeeded in detect optically the spin accumulation generated by injection of non-polarized charge current at nonmagnetic metal/oxide interface [3, 4].

Up to now, I have succeeded in investigating magnon phonon coupling via inverse Edelstein effect and demonstrate the detection of spin accumulation with MOKE system. For the next step, I will focus our study on direct experimental demonstration of spin rotation coupling, and expand magnon phonon coupling study with other different types of acoustic phonons. The success of this project will bring us the original new method of generation of spin current, advance the understanding of spin conversion phenomena, and gives further insight towards future electronic devices.

This thesis is structured as follows:

In chapter 1, I introduce the generation of surface acoustic waves, fabrication processes of acoustic spin pumping devices and the mechanism of acoustic phonon driven magnetic dynamics. Besides, I explain the characterization of magnetic dynamics driven by the surface acoustic wave.

In chapter 2, the spin conversion in Rashba type system is introduced, and the experiment results of inverse Edelstein effect induced by magnon phonon coupling are discussed.

In chapter 3, the future direction is introduced, which focus on the optical characterization of spin accumulation induced by spin rotation coupling. The preliminary results obtained by numerical simulation are presented.

magnetic-field-induced polarisation suppression in TbMn₂O₅ is examined and compared to the multiferroic behavior of YMn₂O₅.

Chapter 1

Acoustic ferromagnetic resonance

Methods for generation of spin current and its conversion to electrical charge current has been vigorously studied in recent years, mainly based on physical phenomena at the nanoscale [1]. Generation of spin current is nevertheless transferring angular momentum to spin. In the presence of magnetic materials, spin currents can be generated by magnon-photon or magnon-phonon coupling. Both are based on the excitation of ferromagnetic resonance, precession motion of magnetization along field direction to transfer angular momentum.

The magnon-phonon coupling can be achieved by passing surface acoustic waves (SAWs) across ferromagnetic layers. Due to magneto-elastic effect [5, 6], waves inducing periodic elastic deformation of ferromagnetic film drives precessional magnetization dynamics in the presence of magnetic fields, producing spin current into nonmagnetic layers. In general, this coherent magnetic excitation driven by acoustic waves is termed as acoustic ferromagnetic resonance (A-FMR), analogous to the most common ferromagnetic resonance which is operated by electromagnetic waves (photons).

Once the acoustic ferromagnetic resonance is excited, the energy transfer from acoustic waves to ferromagnetic materials can be detected as significant damping of SAWs. Thus, in this study, the analysis of magnon-phonon coupling is mainly based on the absorption spectrum of SAWs and its dependence on the angle of in-plane external magnetic fields as presented in section 1.4.

In the following sections, the basic concept of surface acoustic wave and magnon phonon coupling are discussed. Then the fabrication process of devices is introduced. After that, experiment results are shown, followed by a discussion and a conclusion.

1.1 Surface acoustic wave generation

Surface acoustic waves are one category of elastic waves. Different from bulk waves, they travel only on the surface with an amplitude decaying exponentially from surface to bulk. According to the geometry of the deformation field concerning the surface, surface acoustic waves are classified as Rayleigh waves, Love waves, lambda waves and so on. In this study, we employ Rayleigh waves by considering the coherency of its strain field and the significant long traveling distance, as these two properties are undoubtedly the footstone of this study.

Considering its low damping and high compatibility, in general, SAWs are ubiquitously utilized in radio-frequency electronics circuits, functioning as signal filters, resonators, and among other applications.

In these devices, SAWs are generated by using the periodic metal electrodes (well known as interdigital transducers, IDTs) patterned on piezoelectric materials. By applying radio-frequency voltage, IDTs couple electric field with elastic field, converting electrical oscillation to lattice vibration, launching SAWs propagating on substrates.

This phenomenon, generally named as an inverse piezoelectric effect, happens only in certain anisotropic crystals. Due to the lack of structural inversion symmetry, unbalanced internal force can be easily guided by polarization, which, in a macro view, is visualized as electric field inducing strain on materials (see figure 1.1 b). Vice versa, the reciprocal effect used to produce electric field by applying stress to crystals is the direct piezoelectric effect (see figure 1.1 a). However, this effect is negligible in most of the materials. The reason behind those significant piezoelectric responses remains a mystery. Up to now, only limited numbers of crystal possess strong piezoelectricity. In this experiment, we choose Lithium Niobate (LiNbO_3) substrate because of its high Q-factor and robust piezoelectric response.

In summary, as schematically depicted in 1.1, by employing a reverse piezoelectric effect, SAWs are launched along the surface. Then, once reach the second port, SAWs induces an electric signal due to direct piezoelectric effect. Besides, further details of the interdigital transducer fabrication and the characterization of SAWs devices are shown in the section 1.3.1 and 1.3.3 respectively.

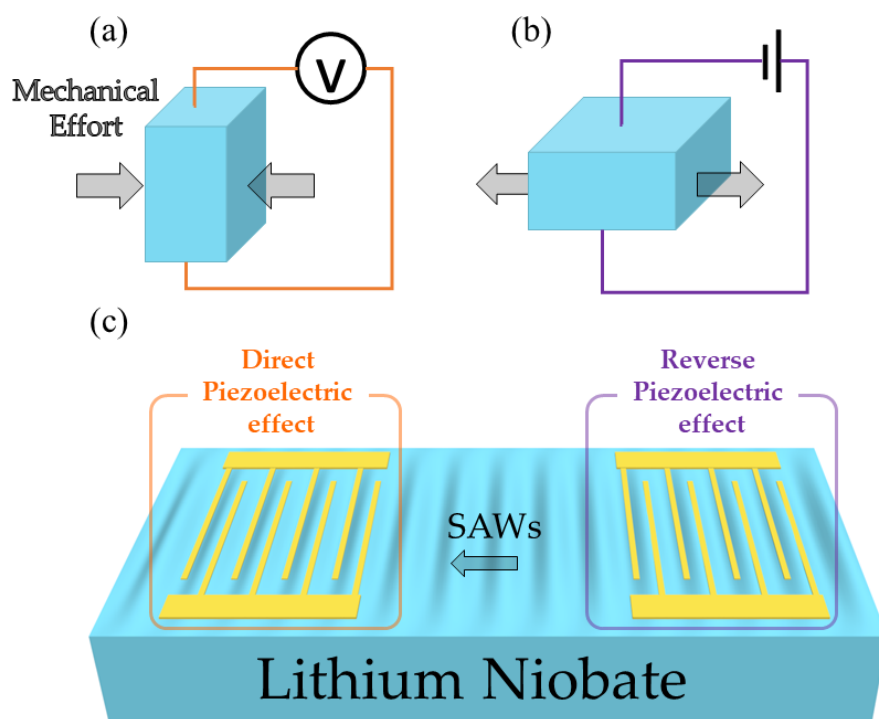


Fig. 1.1 Schematic of direct piezoelectric effect (a), reverse piezoelectric effect (b), and an integral device allowing both direct and reverse effects to take place (c).

1.2 Magnetoelastic magnetization dynamics

Due to inverse piezoelectric effect, by applying radio frequency voltage on IDTs, SAW is excited and propagate along the surface along the x-axis (see figure 1.8), driving a time-dependent strain field $\epsilon(t)$ in the lattice, inducing a time-varying contribution to the magnetic anisotropy in the ferromagnetic layer via magnetoelastic effect. Once the waves couple with the ferromagnetic material, manifested anisotropy field excites a precessional motion of magnetization M around the direction of an external magnetic field H , enabling acoustic ferromagnetic resonance. The schematics of acoustic ferromagnetic resonance is depicted in figure 1.2

In this section, the acoustic phonon driven magnetization is introduced. Before moving to the phonon driven ferromagnetic resonance, the section starts with a standard model of ferromagnetic resonance with a brief introduction. Moreover, then, it moves to the mechanism of phonon driven ferromagnetic resonance and the unique feature compared with photon triggered ferromagnetic resonance.

Different from paramagnetic and diamagnetic materials, there is a spontaneous ordering of magnetic moments. Moreover, the collective alignment of these magnetic moments gives a macroscopic magnetization M .

While an external magnetic field H is applied at an angle α to the x axis and an angle β to the z -axis, the magnetization M is aligned at an angle ϕ and θ respect to x and z axis. The orientation of M follows the distribution of magnetic anisotropy which is calculated by minimizing thin films magnetic free energy density F .

$$F_{DC} = -\mu_0 H \cdot m + B_d m_z^2 + B_u (u \cdot m)^2 \quad (1.1)$$

Where $m = \{m_x, m_y, m_z\}$, represents the magnetization direction vector, and B_d and B_u is the out of plane and in plane spontaneous anisotropy field of the thin film. As magnetization M always follows the most energetically favorable direction, one can determine it by :

$$\mu_0 H_{eff} = -\nabla_m F^{DC} = \mu_0 (H + H_{aniso}) \quad (1.2)$$

Here, magnetization M is aligned along H_{eff} , and H represent real externally applied a magnetic field, while H_{aniso} is a practical term to describe the anisotropy field. However, this study focuses on is rather than equilibrium state but magnetization

dynamics which follows the classical equation of precession motion, the Landau-Lifshitz-Gilbert equation:

$$\partial_t m = -\gamma m \times \mu_0 H_{eff} + am \times \partial_t m \quad (1.3)$$

Where $\gamma = g\mu_B/\hbar$ is the gyromagnetic ratio, with bohr magneton μ_B and reduced Planck constant \hbar . By solving Landau-Lifshitz-Gilbert equation, one can picture the processing motion of magnetization M along H_{eff} . By including this time dependent contribution $H(t)$ into the initial effective H for the equilibrium state, one can obtain the description of magnetic dynamic as:

$$\mu_0 H_{eff} = -\nabla_m F^{DC} = \mu_0(H + H(t) + H_{aniso}) \quad (1.4)$$

. In general, microwave photon is used to induce the time-dependent contribution $H(t)$, In a more intuitive way to understand this coupling between microwave photon and magnon, one can consider angular momentum conservation rule for the system, as the external injected angular momentum choose to relax in materials as a spin. Analogous to this, one can further imagine the possibility of the gigahertz acoustic phonon can work in the same way. Similar to the piezoelectric effect described in the last section, elastic tensor can also couple with magnetic anisotropy due to magnetoelastic effect (also known as inverse magnetostrictive effect or Villari effect). Instead of triggering as a $H(t)$, time dependent deformation field of ferromagnetic add a $H_{aniso}(t)$ to the equation. In the end, triggering the processing motion of M around H_{eff} as:

$$\mu_0 H_{eff} = -\nabla_m F^{DC} = \mu_0(H + H_{aniso} + H_{aniso}(t)) \quad (1.5)$$

The $H_{aniso}(t)$ driving field is given by taking in account the magnetoelastic coupling energy density $F_{coupling}$.

$$H_{aniso}(t) = -\nabla_m F_{coupling}(t) \quad (1.6)$$

Following the derivation process describe in [7], by correlating the elastic tensor and magnetoelastic coupling tensor, one can obtain:

$$[\mu_0 h_{rf}(t)(\theta)]^2 = [b_1 \varepsilon_{xx0} \sin\theta \cos\theta + b_2 \varepsilon_{zx0} \sin\theta]^2 \quad (1.7)$$

where, $b_{1(2)}$ is the magneto-elastic coupling constant, $\varepsilon_{xx0(zx0)}$ represents the longitudinal strain (shear strain) induced by SAW, and θ refers to in-plane static magnetic field orientation as depicted in figure 1.8.

Note that $h_{rf}(t)$ presented here only takes into account the component transverse to H_{eff} of $H_{aniso}(t)$ as only this component play an active role in exciting ferromagnetic resonance.

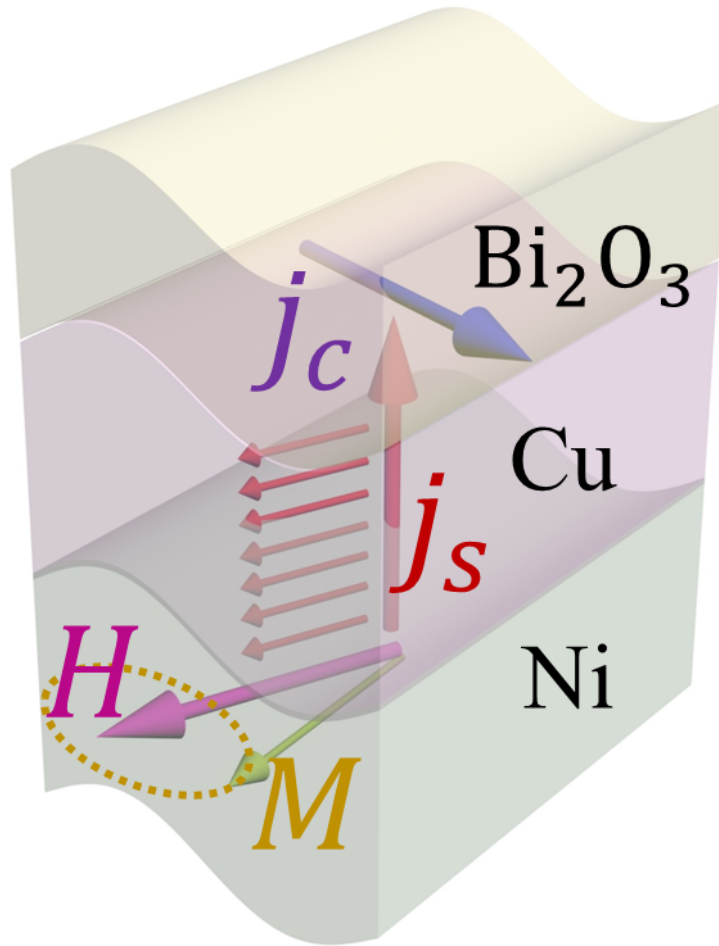


Fig. 1.2 Acoustic spin pumping (ASP) mechanism acting in a trilayer formed by Ni/Cu/Bi₂O₃.

1.3 Device fabrication process

The basic components of our devices are:

1. Interdigital transducer for generation of surface acoustic waves
2. Efficient piezoelectric material for voltage to acoustic field conversion.
3. Ferromagnetic material for the generation of spin current by the interaction with the SAW.

In the investigation of the coupling between phonon and magnon, we employ a piezoelectric /ferromagnetic hybrid device, consist of a piezoelectric substrate, LiNbO_3 , for the efficient generation of the SAW and magneto-elastic material, Ni, for the interaction of magnon and phonon. As illustrated in figure 1.3 one pair of IDTs is patterned on a LiNbO_3 substrate with an in-between ferromagnetic layer to study the absorption spectrum,

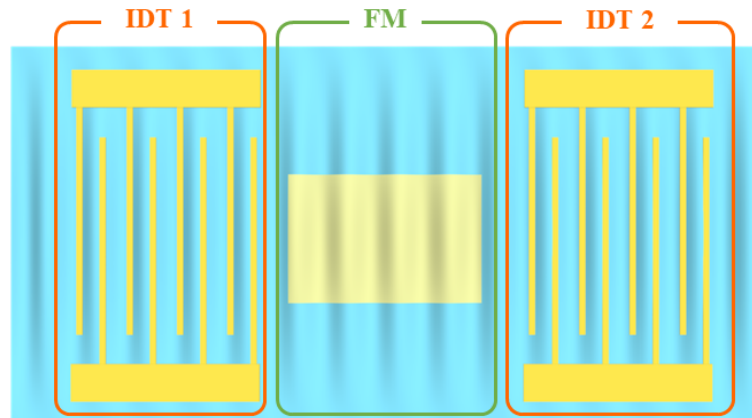


Fig. 1.3 Top view of device layout. IDT1 and IDT2 are designed for investigating the absorption spectrum of SAW while center FM layer is for the interaction of phonon and magnon.

The devices fabrication consists of 4 steps. Firstly, the strips shape interdigital transducers with dimension of $100\mu\text{m}\times 400\text{nm}$ are patterned by electron beam lithography (EBL) under 100kV and beam current of 100pA on LiNbO_3 substrate, and metallization is subsequently carried out with 5nm Ti and 20nm Au by electron beam evaporation. To ensure the IDTs are well fabricated, scanning electron microscopy (SEM) is performed. figure 1.6 shows SEM image of fabricated IDTs. Secondly, the contacts for IDTs are defined by maskless photo-lithography followed

by deposition of 5nm Ti and 200nm Au by electron beam evaporation. Thirdly, the Ni(10nm)/Cu, Ag(20nm)/Bi₂O₃(20nm) multilayer structures are patterned by maskless photo-lithography followed by deposition by electron beam evaporation. Fourthly, contacts are defined by maskless photo-lithography followed by deposition of 5nm Ti and 200nm Au by electron beam evaporation. 1.4

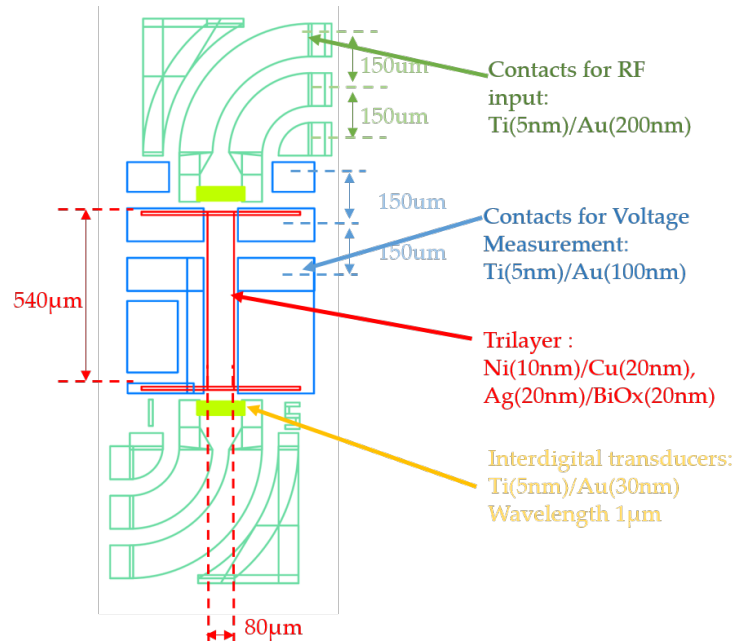


Fig. 1.4 CAD design of sample. Layout of sample

Because of their importance, the IDTs patterning and deposition of trilayer are described exclusively in this section.

1.3.1 IDTs patterning by using Electron beam lithography

To generate coherent gigahertz acoustic phonon, nanometer wide electrode is an indispensable element. Towards this purpose, electron beam lithography is used for patterning IDTs, considering its much higher resolution compared with standard optical lithography.

The IDTs patterning mainly consist of 3 steps:

1. Coating substrate with electron sensitive resist.

Spin coating is used in this process, followed by post-baking on hot plate. Note that rotation speed at 4000 rotation per minutes is to obtain film thickness

at 300nm and the 90-second post-baking at 180 °C for hardening the resist. The details about the parameters are listed in Table 1.1. The resist used in this case is isopolymethyl-methacrylate with molecular weight 950 and diluted with anisole 4% (purchased from Microchem Co. Ltd.), generally abbreviated as 950PMMA A4. The ESPACER (electric spacer) used in this process is for avoiding the charge accumulation on the substrate. It sometimes causes extra damage to the machine. There is no post-baking after ESPACER coating as it does not play a crucial role in the lithography process.

Table 1.1 Resist preparation

Resist	Spin coating		Baking	
	Rotation(RPM)	Time(s)	Temperature(°C)	Time(s)
PMMA	500	10	180	90
	4000	40		
ESPACER	500	10		
	2000	20		

2. Exposing substrate with an electron beam.

Firstly, the pattern is predefined in CAD as shown in figure 1.5 and later converted in CEL file in an electron beam lithography system. Secondly, the substrate is exposed accordingly with 100pA electron beam with a dose parameter equals to 0.25. Note that the electron beam lithography system employed is Elionix7700. Besides, as the sensitivity of the resist varies according to the storage environment, the optimization process of exposure parameters is recommended.

3. Developing patterns with a corresponding chemical solution.

As detailed in table 1.2, the development process contains three steps. The first step, cleaning the substrate with deionized water, is mainly for removing the ESPACER. If ESPACER is not used, this step can be skipped. The real development process is in the second step, soaking substrate in a chemical solution which is composed by Methyl isobutyl ketone (MIBK) and isopropyl alcohol (IPA) (mixed following the ratio of 4:1). After 20 seconds of development, the substrate is transferred to be soaked in IPA for the 30s to remove the exposed part of resist.

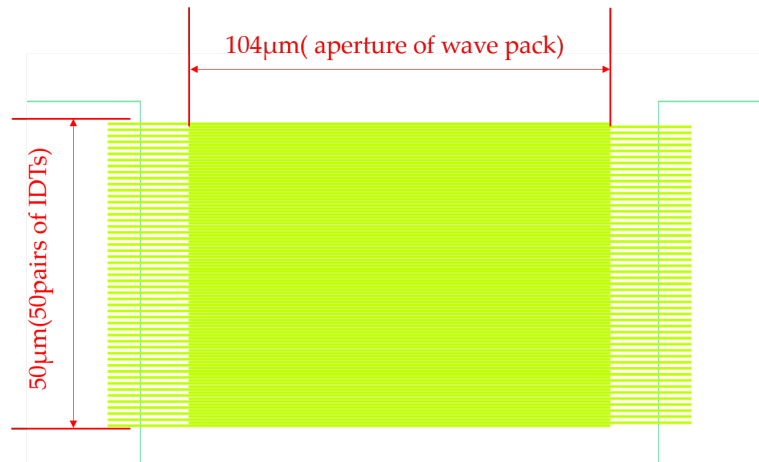


Fig. 1.5 A example of IDTs design in CAD

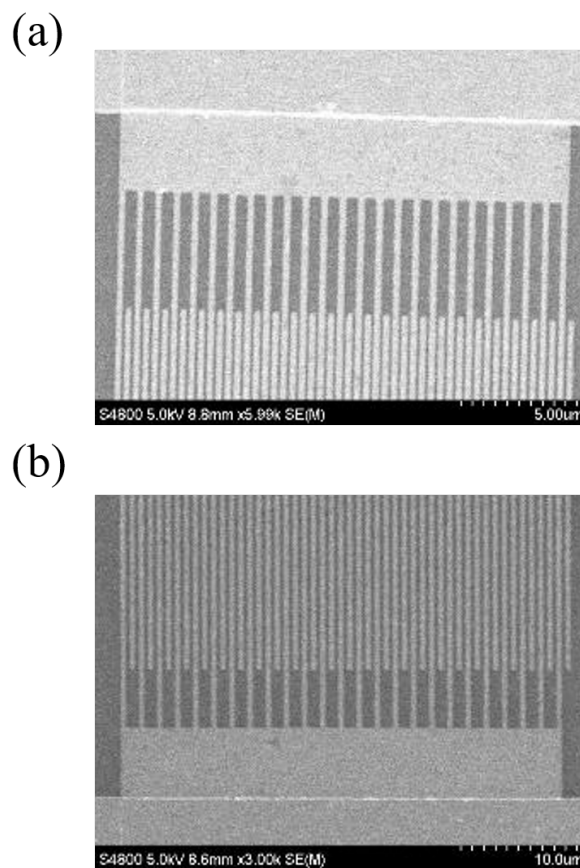


Fig. 1.6 Scanning electron microscope image(SEM) of fabricated interdigital transducers. (a) and (b) correspond to the devices with center-to-center spacing 400nm and 800nm respectively.

Table 1.2 Development

Chemical solution	Time(s)
DI.Water	30
MIBK:IPA	20
IPA	30

1.3.2 X-ray crystallography

To confirm the crystalline information at Cu/Bi₂O₃ and Ag/ Bi₂O₃ interfaces, we used the grazing incident X-ray diffraction method. As shown in Fig. S2, at the interfaces, amorphous Bi₂O₃ is observed, and both Cu and Ag show preferential crystallinity at (111) which is similar to the orientation in previous reports of Rashba interfaces of Ag (111)/Bi [1].

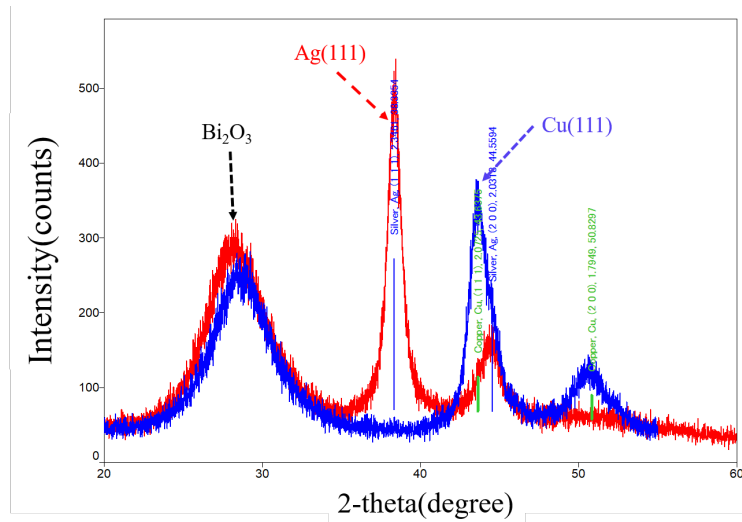


Fig. 1.7 XRD spectroscopy characterization at 0.45° incidence angle. The blue line and red line are the results for Cu/Bi₂O₃ and Ag/Bi₂O₃, respectively. The same broad peak 28° shown in both blue and red line are characteristic peaks of amorphous Bi₂O₃. Moreover, the next two peaks, 38.3° in the red line, 43.6° in the blue line, represent the characteristic peak of Ag (111) and Cu (111), respectively.

1.3.3 Experimental setup

After the fabrication, the samples were mounted on a stage attached with a shaft encoder, allowing precise rotation of in-plane magnetic field.

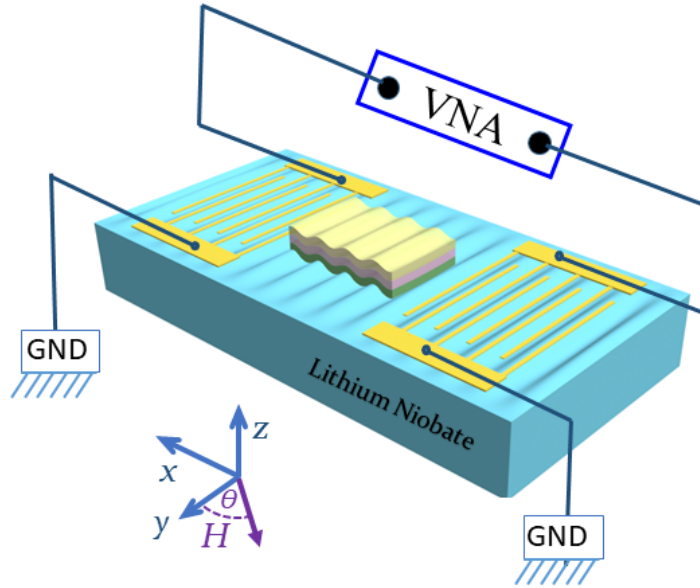


Fig. 1.8 Illustration of experiment setup. The surface acoustic waves are generated by applying RF voltage on interdigital transducers and the longitudinal voltage and transverse voltage are measured while applying an external magnetic field \mathbf{H} at an angle θ .

To confirm SAW is well excited, we first measure transmission between input and output ports with Network Analyzer N5225b. Time gating method is used in the characterization of IDTs for ruling out noise caused by spurious electromagnetic waves signal. With time gating method, the false signal is reduced significantly, as shown in figure 1.9.

1.4 Experimental results and discussion

The spin current generated by acoustic ferromagnetic resonance can be analyzed by studying the absorption spectrum of acoustic waves in the ferromagnetic layer. As schematically illustrated in figure 1.8, we first characterize the absorption of SAW by using a vector network analyzer (VNA), while varying the in-plane external magnetic field angle. One of examples is shown in figure 1.10

Absorption of the SAW is characterized by systematically measuring the transmission coefficient $|\overline{S}_{21}|$ as a function of in-plane static magnetic field magnitude and angle θ , as illustrated in figure 1.8. Figure 1.11 shows the magnetic field angle dependence (θ) at the resonance peak of the acoustic ferromagnetic resonance. We

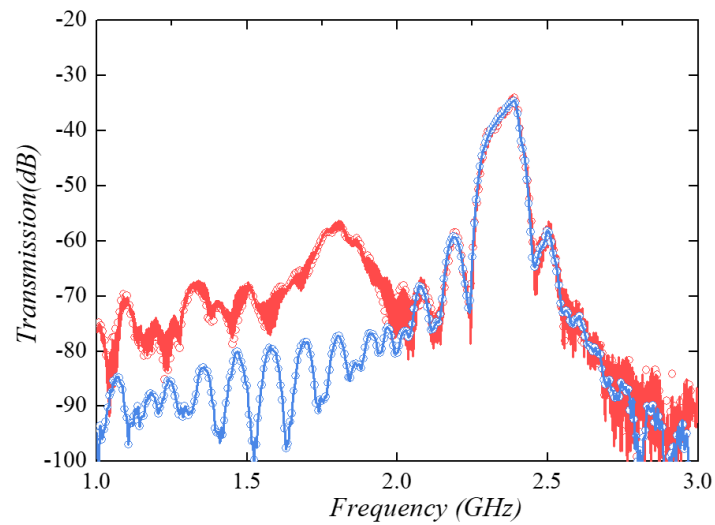


Fig. 1.9 An example of transmission spectrum measured with (Blue line) and without (Red line) time gating method. Note that this one does not corresponding to the device used in section 1.3

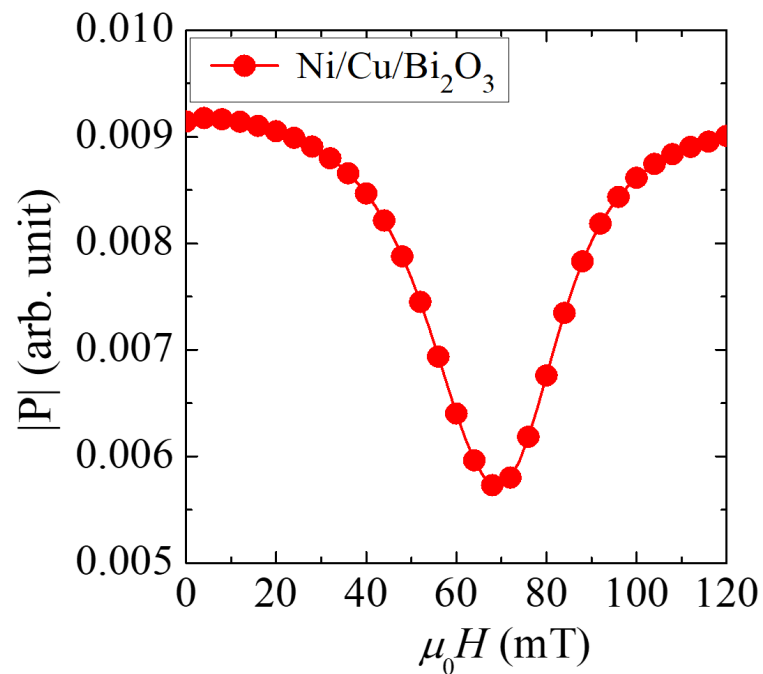


Fig. 1.10 AFMR spectrum

observe a four-fold butterfly shape signal with the first maximum located at $\theta = 45^\circ$. Previous reports showed a four-fold symmetric dependence of SAW absorption with the angle formed between SAW \mathbf{k} -wavevector and in-plane magnetic field, having maximum absorption at 45° , and it is considered as the fingerprint of acoustic-FMR [5, 6]. The asymmetry between the top and bottom side of the four-fold symmetry indicates the non-negligible interference of magneto-elastic couplings of shear waves and longitudinal waves (figure 1.11). Magnetization dynamics induced by Rayleigh SAW are composed by a longitudinal wave and shear wave motion components which is perpendicular to each other ($\pi/2$ dephasing), forming ellipsoidal oscillations. When the SAW direction vector \mathbf{k} is reversed, the ellipsoidal motion is reversed, which is accompanied by a sign change of the shear strain component ε_{zx0} . Magnetoelastic coupling by interference of longitudinal (ε_{xx0}) and shear wave (ε_{zx0}) can be described by equation 1.7 which directly elucidates the excitation efficiency of FMR, which is proportional to the SAW absorption $\Delta P(\theta) \propto [\mu_0 h_{rf}(\theta)]^2$ (see equation 1.5).

Recently, the microscopic origin of this asymmetric mechanism has been reported, and it has been ascribed to the simultaneous breaking of time reversal and spatial inversion symmetries [7]. Both, time reversal and spatial inversion symmetry are broken at our hybrid device. The resultant asymmetry is particularly evident for Ni/Ag/Bi₂O₃ in figure 1.11. The ratio of longitudinal and transverse magnetoelastic coupling in Ag is larger than Cu, inducing larger anisotropies [8].

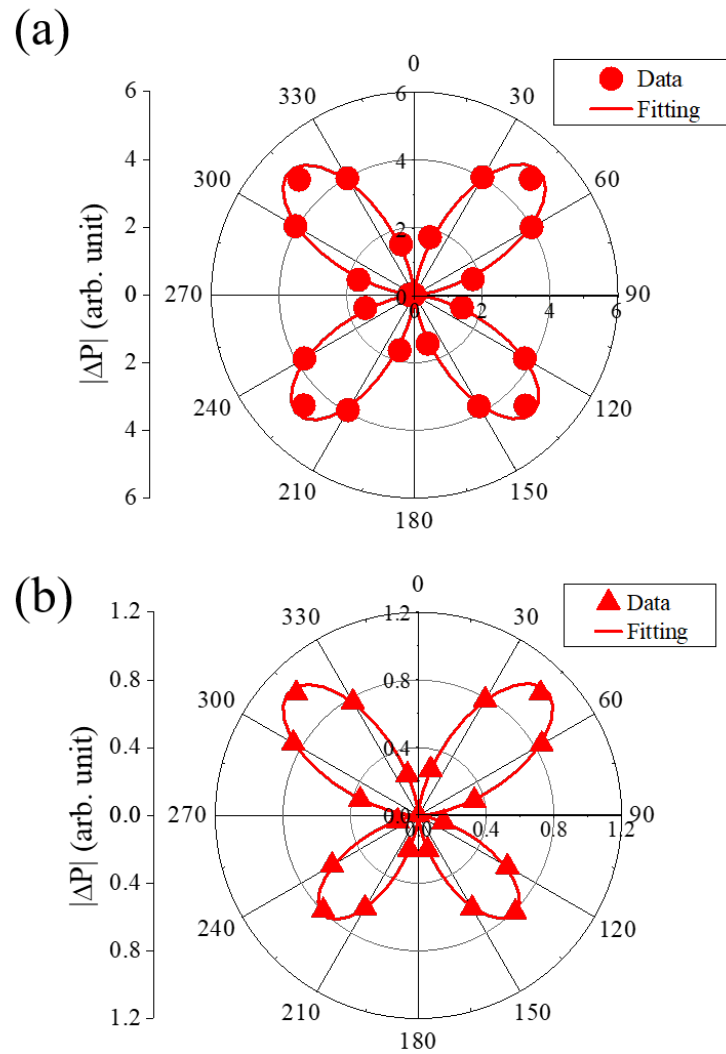


Fig. 1.11 Polar graph of damping of SAW due to acoustically excited FMR measured on (a): Ni/Cu/Bi₂O₃ and (b): Ni/Ag/Bi₂O₃, varying applied magnetic field angle θ .

1.5 Conclusions and outlook

Here, the magnon-phonon coupling has been experimentally investigated in this chapter. Due to the excitation of ferromagnetic resonance, SAWs shows a significant magnetic dependent damping, which allows studying the coupling precisely and systematically. As shown in section 1.4, the experiment result agrees well with the theoretical prediction, showing butterfly shape angular variation of the signal. Moreover, the additional finding of The difference between the angular variation pattern from Ni/Cu/Bi₂O₃ and Ni/Ag/Bi₂O₃ stay an interesting unexplored phenomenon which requires further study.

However, the method presented in this chapter can be improved further. Instead of indirect studying the coupling through analyzing the transmission spectrum, the next chapter demonstrates a direct way to visualize magnon phonon coupling. As schematically shown in figure1.2, due to excitation of acoustic ferromagnetic resonance, spin current is injected into the adjacent nonmagnetic layer, Cu/(Ag). Then, due to the inversion spatial symmetry breaking at the interface between Cu (Ag) and Bi₂O₃[9, 3, 10], the system converts spin current into charge current via inverse Edelstein effect, inducing a magnetic field dependent voltage V , detected in longitudinal and transverse geometries. This method allows directing a study on the central multilayer system, instead of treating it as a black box. The detail of this method is described in the chapter2.

Chapter 2

Spin to charge conversion induced by magnon-phonon coupling

Since last century, spin conversion, the key concept of Spintronics, has been intensively investigated in order to gain a deeper understanding of spin dynamics and enriching the functionalities of electronic devices. It describes various intriguing phenomena taking place at nanoscale between electricity, light, sound, vibration, heat, etc., based on the interconversions mediated by spin [1].

Among the conversion phenomena mentioned above, the interconversion between charge and spin is the one most widely employed conversion. In 1971, Russian physicists M. I. Dyakonov and V. I. Perel published a theoretical framework [11], predicting the appearance of spin accumulation on the lateral surface of a conductor when current flows through it. This transport phenomenon, later term as spin Hall effect (SHE), was experimentally demonstrated by Bakun et al. in 1984 [12].

Different from her, recent reports show efficient spin to charge current conversion at interfaces with spatial inversion asymmetry between two nonmagnetic materials [13, 9]. Spatial inversion asymmetry induces a built-in electric potential and spin-orbit coupling at surfaces and interfaces, the so-called Rashba spin-orbit coupling. Here, the spin to charge conversion mechanism is known as inverse Edelstein effect (IEE).

In this study, interfacial Rashba systems between nonmagnetic metal and bismuth oxide are employed in the direct investigation of the magnon phonon coupling. The contents of this chapter start from the fundamental concept of Rashba spin-orbit coupling and inverse Edelstein effect, followed by the experimental observation of spin to charge conversion induced by magnon-phonon coupling.

2.1 Rashba splitting

With the increasing need for more flexible compatibility of Spintronics devices with the circuit, the manipulation of spin polarization without external magnetic field attracts great interest. Towards this aim, the Rashba system is one of the most promising approaches. It depicts a scenario that, in a two-dimensional electron system, spatial inversion asymmetry (SIA) lifts spin degeneracy, resulting in a characteristic band dispersion. In general, it is described by a so-called Bychkov and Rashba model (BR) [14]:

$$\hat{H} = \frac{\hbar^2}{2m^*}k^2 + \alpha_R[\vec{\sigma} \times k]\vec{v} \quad (2.1)$$

The dispersion law follows[15]:

$$E_{\pm}(k) = E_0 + \frac{\hbar^2 k^2}{2m^*} \pm |\alpha_R||k| \quad (2.2)$$

where \hbar is the reduced Plank constant, m^* is the effective mass, k represents 2D quasimomentum, α is coefficient (later known as Rashba parameter), $\vec{\sigma}$ is Pauli matrix, \vec{v} is a unit vector which is directed in the normal to heterojunction.

And the Rashba parameter α_R is calculated as [16]:

$$\alpha_R = \left(\frac{2}{c^2}\right) \int \frac{\partial V}{\partial z} \psi^2 dz \quad (2.3)$$

where c is the speed of light, $\partial V/\partial z$ is potential gradient, ψ^2 is electron density distribution with boundary condition $z = 0$ at the center of interface region. At the very beginning, this linear term is measured by spin-flip Raman scattering [17] and also observed via magnetotransport measurement [18]. In fact, most important informations of the splitting are summarized in Rashba Parameter. The energy of Rashba spin orbit interaction and the splitting direction are reflects on the amplitude and sign of the Rashba parameter [15].

Even though this model is initially developed for semiconductors, the Rashba-Bychkov model has been successfully applied to surface state and interface state of metallic systems. Notably, in the electronic structure of a clean surface of heavy metal and heavy-element interface alloy, particularly giant Rashba spin-splitting has been observed.

However, the origin of these giant Rashba type splitting is still under debate. Most well-accepted concepts claim the vital contribution from strong spin-orbit interaction, spatial inversion asymmetry and structural parameters [19, 20]. Despite the hot debate, manipulating spin in Rashba systems has been intensively studied. In the following sections, an example of the practical usage based on inverse Edelstein effect is introduced (see section 2.2) and followed by the experiment observation (see section 2.3)

2.2 Inverse Edelstein effect

It was predicted by Edelstein in 1989 [21] that the absence of "up-down" symmetry in two-dimensional electron systems permits a magneto-electric effect. As mentioned in section 2.1, the spatial inversion asymmetry induces an additional spin-orbit interaction term, allowing a resultant magnetic field (see figure 2.1). Although, in an equilibrium state, the average built-in magnetic field equals to zero, when in a current-carrying state, the drifted electron distribution gives a non-zero magnetic field (see figure 2.1). This non-zero magnetic field is normally termed as spin accumulation which represents the unbalanced chemical potential of the spin state. For simplicity, this phenomenon is generally depicted as a shift of Fermi contour (see figure 2.1 a). The reciprocal effect, it is well known as inverse Edelstein effect describes a scenario that e injection of spin state induces equilibrium state, resulting in electric potential in the plane of two-dimensional electron gas (see figure 2.1 b).

The conversion efficiency, inverse Edelstein length can be expressed by considering Rashba parameter α_R and momentum relaxation time τ_e^{int} at the interface [22]:

$$\lambda_{IEE} = \alpha_R \tau_e^{int} / \hbar \quad (2.4)$$

Back in 2014, Rojas Sánchez and colleagues experimentally demonstrated the spin to charge conversion in a Rashba interface [13]. Since then, Spintronics community has intensively investigated on the spin conversion phenomenon in low dimensional. Most likely, this observation of related phenomenon asks for ultra high-quality films, in order to have to have a well-defined interface structure. This requirement anchors the path of applying this phenomenon to commercial applications.

Different for conventional case, the recent report from Karube and colleagues, shows surprisingly large conversion efficiency in an amorphous oxide (Bi_2O_3) and

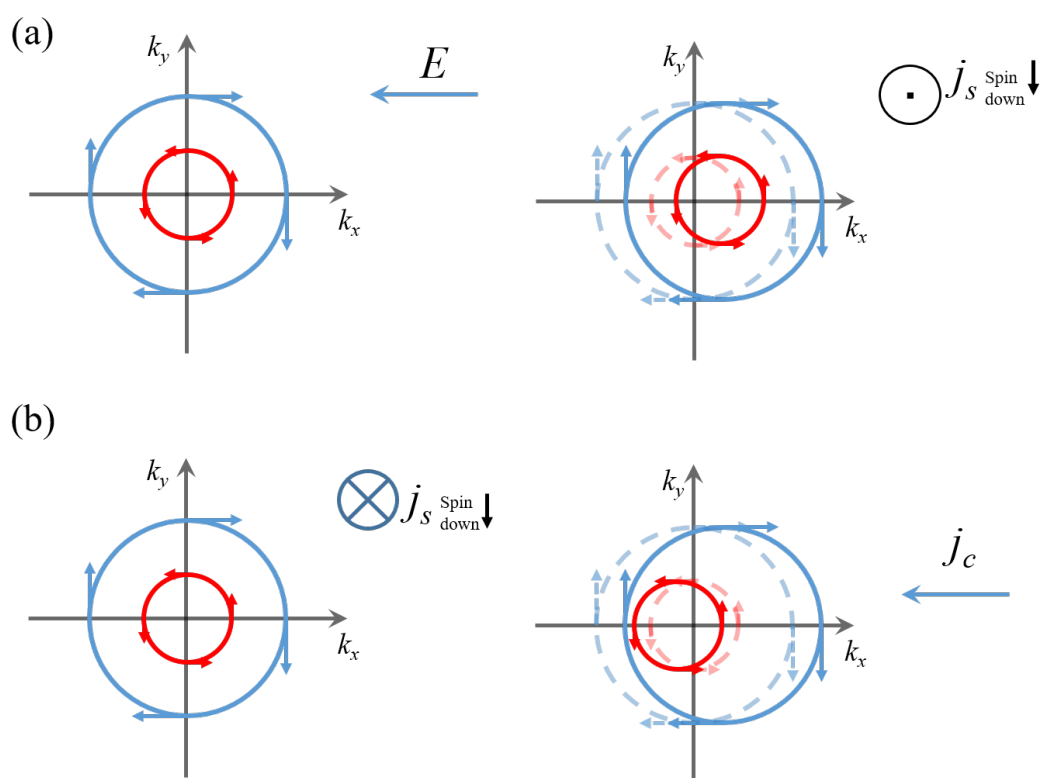


Fig. 2.1 Schematics of direct Edelstein effect (a), and inverse Edelstein effect (b).

copper interface [9]. Later, further study has been done by Tsai and colleagues, showing comparable large conversion efficiency, known as inverse Edelstein length, $0.17nm$ [23], which is comparable to the value estimated for bismuth and silver interface alloy case [13]. This unexpected result easy the path of obtaining materials presenting Rashba type interaction allows a broader and systematical study of this phenomenon [10, 3, 4].

In this study, different from the previously mentioned experiment, rather than microwave, inverse Edelstein effect is induced by magnon-phonon coupling. The results are presented in the following section.

2.3 Experimental results and discussion

Driving of acoustic-FMR produces a spin current which can be injected to adjacent nonmagnetic layers and converted to charge current when spin-orbit interaction exists. In the detection of charge signal induced by inverse Edelstein effect, same devices as presented in the last section are employed, which consist Ni/Cu, Ag/Bi₂O₃ heterostructures.

As the spin configuration at the interface of Cu/Bi₂O₃ has opposite sign compared with Ag/Bi₂O₃, the electric signal from them is supposed to have opposite sign follows the spin text as the interface. This comparison plays an important role in justifying the reliability of the signal, to confirm the signal originating from the spin current. Figure 2.3 shows the magnetic field dependent IEE charge current detected in Ni/Cu/Bi₂O₃ (red circles) and Ni/Ag/Bi₂O₃ (blue triangles) devices, rescaled by their corresponding SAW power absorption, P_{SAW} .

Also, in order to have a complete view of the acoustic spin pumping, the study is extended to the full in-plane magnetic field angle dependence with voltage detection in both, transverse and longitudinal geometries as schematically depicted in figure 2.2.

In this section, the main contents consist of four subsections. Firstly we start with direct experiment results of inverse Edelstein effect signal (section 2.3.1). Secondly, Considering the complexities of the formula used in section 2.3.1, a detail introduction of the formula is explained in section 2.3.2. Thirdly, distribution of electric response, which is induced by IEE, is mathematically converted back into an angular variation of spin currents to track back to the information of magnon-phonon coupling. Fourthly, in the last subsection, we introduce our assumption of the mysterious additional asymmetry which only appears in longitudinal voltage detection results.

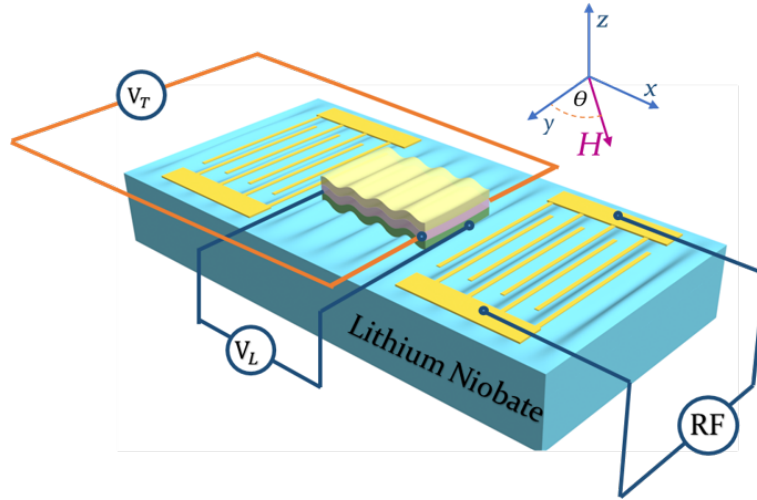


Fig. 2.2 Illustration of experiment setup. The surface acoustic waves are generated by applying RF voltage on interdigital transducers and the longitudinal voltage and transverse voltage are measured while applying an external magnetic field \mathbf{H} at an angle θ .

2.3.1 Inverse Edelstein effect voltage detected in transverse and longitudinal geometries

Because the inverse spin Hall effect is negligible in our device, the spin pumping signal is mainly a consequence of the IEE. Therefore, the opposite sign of the spin pumping signal shown in figure 2.3 reflects the opposite spin-momentum locking configuration at $\text{Cu}/\text{Bi}_2\text{O}_3$ and $\text{Ag}/\text{Bi}_2\text{O}_3$ interfaces, corroborating well the observation from electromagnetic wave induced spin pumping and MOKE [3, 23]. Spin pumping measurements driven by electromagnetic wave FMR contain an asymmetric component due to classical induction effect, the anisotropic magnetoresistance voltage [24]. The induction effect is strongly suppressed in acoustic spin pumping measurements.

Feasibility of acoustic spin pumping was previously reported in a limited range of in-plane magnetic field angles, measured in transverse geometry [25]. We extend our study to the full in-plane magnetic field angle dependence with voltage detection in both, transverse and longitudinal geometries. For transverse geometry we detect the voltage perpendicular to the SAW wavevector \mathbf{k} (V_T in figure 2.4 (a)), while for the longitudinal geometry we detect the voltage parallel to the SAW wavevector \mathbf{k} (V_L in figure 2.4 (c)). figure 2.4 (a, b) shows the magnetic field angle dependence (θ) of the transverse IEE voltage V_T for $\text{Ni}/\text{Cu}/\text{Bi}_2\text{O}_3$ (a) and $\text{Ni}/\text{Ag}/\text{Bi}_2\text{O}_3$ (b). Since the

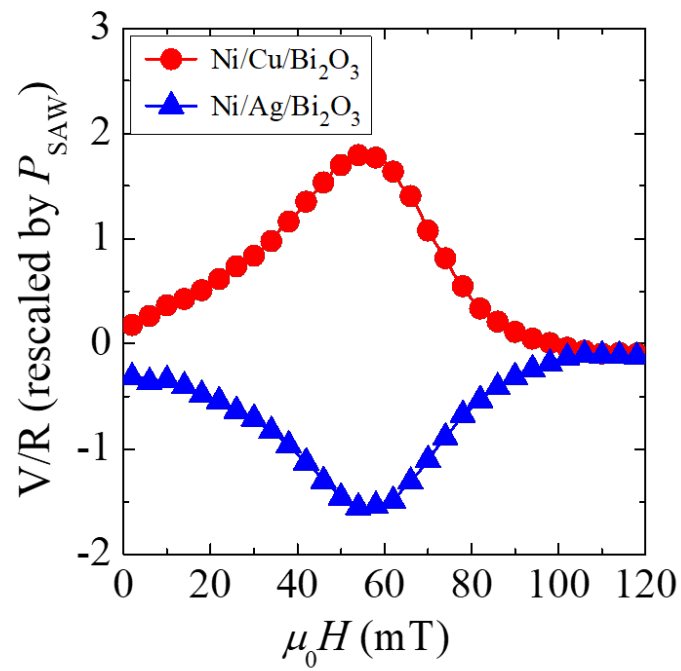


Fig. 2.3 Longitudinal signal measured on Ni/Cu/Bi₂O₃ (red circles) and Ni/Ag/Bi₂O₃ (blue triangles) devices depending on the magnetic field amplitude at $\theta = 240^\circ$. The opposite sign of the signal reflects the opposite configuration of spin text at the Fermi contour

V_T mainly depends on the excitation efficiency of FMR and the projection angle of the spin current onto the Rashba interface, the top and bottom side asymmetry presented in SAW absorption is also reflected in the transverse voltage. For fitting our data, as the SAW damping in longitudinal direction does not affect the transverse potential in our device, the longitudinal component of $\mu_0 h_{rf}(\theta)$ has negligible influence in our spin pumping signal, and we can only consider the transverse component of excitation $|\mu_0 h_{rf}| \sin(\theta)$ in

$$V_T(\theta)/R = C_1 [\mu_0 h_{rf}]^2 \sin(\theta) \quad (2.5)$$

We repeat our acoustic spin pumping measurements now with longitudinal voltage detection. Figure 2.4 (c,d) shows the magnetic field angle dependence (θ) of the longitudinal IEE voltage V_L for Ni/Cu/Bi₂O₃ (c) and Ni/Ag/Bi₂O₃ (d). Due to the damping of SAW in the propagation direction, it is possible to observe influence of the transverse excitation component in the V_L , adding an amplitude asymmetry in the four fold symmetry. We fit our data by equation 2.6 (detail description is explained in section 2.3.4 equation 2.13:

$$V_L(\theta)/R = [\mu_0 h_{rf}]^2 (C_2 \sin(\theta) + C_3 \cos(\theta)) \quad (2.6)$$

We also observe an additional asymmetric component in figure 2.4 (c, d) which has not been previously reported. This asymmetric component is described by the non-symmetric charges distribution at the position of our electrodes when varying the magnetic field angle. The charge distribution is dictated by the IEE electric field \mathbf{E} which is proportional to the flow direction of spin current \mathbf{J}_s and its spin polarization σ_s , such that $\mathbf{E} \propto \mathbf{J}_s \times \sigma_s$ [26]. Hence, the asymmetry is the resultant of the projection of spin polarization σ_s in transverse and longitudinal geometries and the damping of SAW in the propagation direction (see section 2.3.4).

Magnitude of spin current generated via magnon-phonon coupling in our samples, can be estimated by equation 2.7 [13]:

$$J_s = \frac{V(\theta)}{\lambda_{IEE} w R \sin \theta} \quad (2.7)$$

where λ_{IEE} is the IEE length, w is the sample width and R the electric sample resistance. For our Cu/Bi₂O₃ we have $\lambda_{IEE} = -0.17 \text{ nm}$ [23], $w = 10 \mu\text{m}$, $R = 42.87 \Omega$.

We obtain a spin current $J_s = 1.648 \times 10^8 A/m^2$ for $V_T(60^\circ)$ of Cu/Bi₂O₃ in figure 2.4(a). This spin current density is comparable to commonly reported values for standard spin pumping driven by electromagnetic wave FMR [13, 27, 28]. Full angle dependence of spin current is available in section 2.3.3.

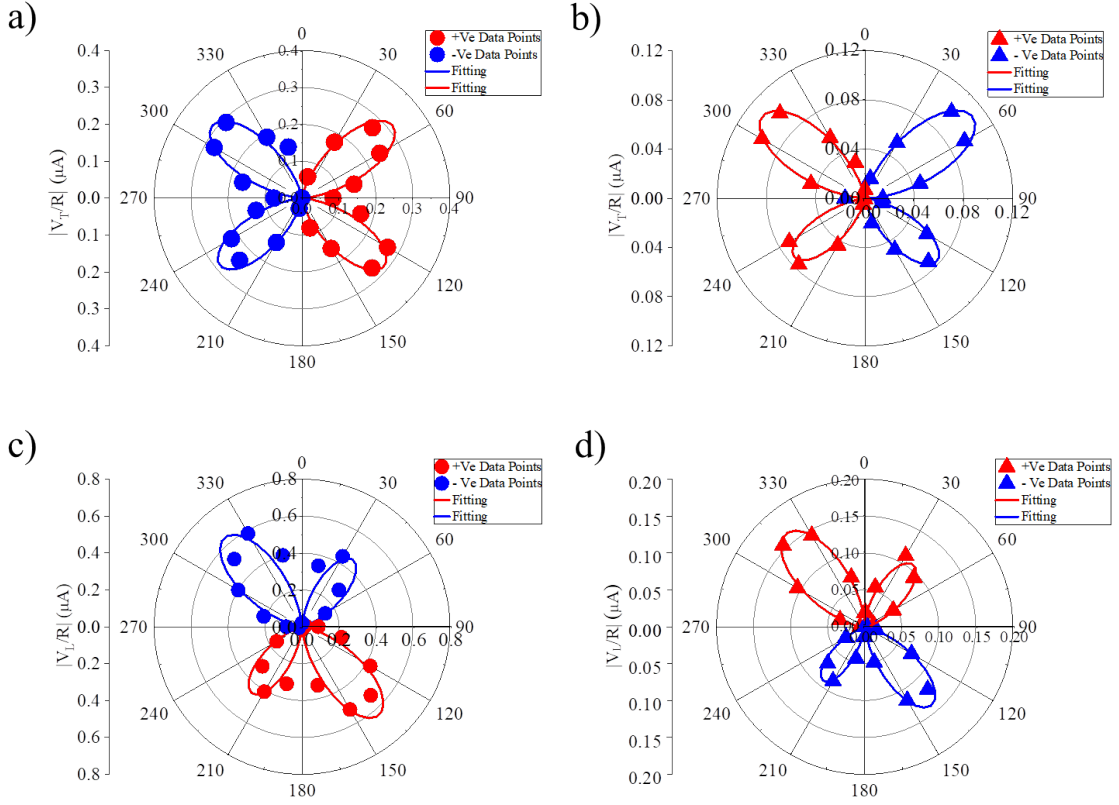


Fig. 2.4 Polar graph of transverse signal measured on (a): Ni/Cu/Bi₂O₃ and (b): Ni/Ag/Bi₂O₃, varying applied external magnetic field angle θ . Polar graph of longitudinal signal measured on (c): Ni/Cu/Bi₂O₃ and (d): Ni/Ag/Bi₂O₃, varying applied external magnetic field angle θ .

2.3.2 Description of fitting formula for IEE voltage detection

In order to study the angular variation of inverse Edelstein effect (IEE) voltage due to the SAW driven magnetic dynamics, we used the following fitting formula 2.8 adapted from Ref [29, 26]

$$V_T(\theta)/R = [\mu_0 h_{rf}]^2(\theta)(C_1 \sin(\theta)) \quad (2.8)$$

Where $V_T(\theta)$ is the transverse voltage signal detect on sample, R is the electric resistance, $\mu_0 h_{rf}$ is described as equation 1.5 and C_1 is:

$$C_1 = \frac{\omega_f \hbar \lambda_{IEE} w \text{Re}[g_{eff}^{\uparrow\downarrow}] P}{16\pi(\Delta H)^2} \quad (2.9)$$

Where P is ellipticity correction factor calculated by following equation 2.10:

$$P = \frac{\omega_f [2\pi\gamma_g M_s + \sqrt{4(\pi\gamma_g M_s)^2 + (\omega_f)^2}]}{2(\pi\gamma_g M_s)^2 + (\omega_f)^2} \quad (2.10)$$

Where $\omega_f = 2\pi f$, is angular frequency, γ_g is gyromagnetic ratio of electrons, \hbar is reduced Planck's constant, λ_{IEE} is the inverse Edelstein length, w is the width of the sample, $\text{Re}[g_{eff}^{\uparrow\downarrow}]$ is the real part of spin mixing conductance (we take $\text{Re}[g_{eff}^{\uparrow\downarrow}] = 8.27 \times 10^{18} m^{-2}$ from Ref [23]), ΔH is the half of the linewidth (15.351 mT), M_s is saturation magnetization of nickel (0.61T). Based on fitting, we obtain angular variation of A-FMR driven effective field for Ni/Cu/Bi₂O₃ as following 2.11:

$$[\mu_0 h_{rf}(\theta)]^2 = [1.601 \sin\theta \cos\theta + 0.014 \sin\theta]^2 \quad (2.11)$$

2.3.3 Angular variation of spin currents generated by acoustic ferromagnetic resonance

The value of the measured voltage signal is used for the calculation of spin current density. For this purpose, we adapted the equation from Ref [13] according to our experiment. The density of spin current (J_s) injected into the interface is

$$J_s = \frac{V(\theta)}{\lambda_{IEE} w R \sin\theta} \quad (2.12)$$

Where $V(\theta)$ is the voltage signal detected while the magnetic field is applied at angle θ , λ_{IEE} is the inverse Edelstein length according to Ref [23] (0.17nm and 0.15nm for Cu/Bi₂O₃ and Ag/Bi₂O₃ interface, respectively), w is the width of the sample (10 μm for our samples) and R refers to the electric resistance of sample (42.87 Ohms,

71.56 Ohms for Ni/Cu/Bi₂O₃ and Ni/Ag/Bi₂O₃ interface, respectively). The angular variation of spin current in Ni/Cu/Bi₂O₃ and Ni/Ag/Bi₂O₃ is plotted in figure 2.5.

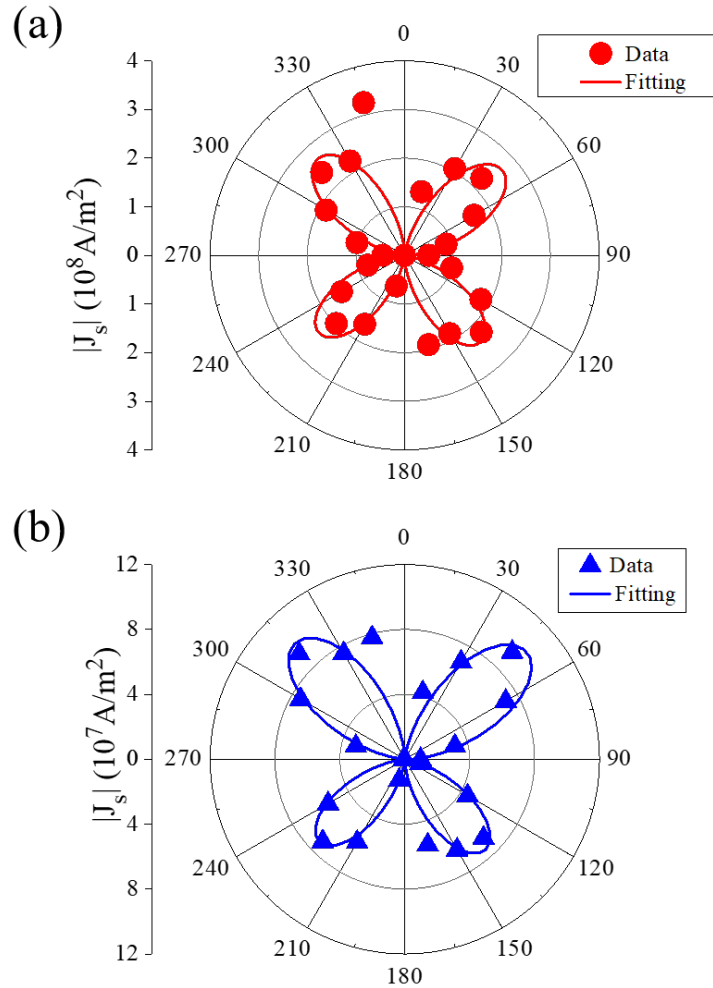


Fig. 2.5 Angular variation of spin current density in (a) Ni/Cu/Bi₂O₃ and (b) Ni/Ag/Bi₂O₃.

2.3.4 Anisotropic distribution of charge potential

Due to the inverse Edelstein effect, the spin current generated by acoustic ferromagnetic resonance induces rearrangement of charge potential on the sample. Different from the normal spin pumping, acoustic spin pumping induces an inhomogeneous distribution of charge potential as depicted in 2.6(a,b). We assigned as the origin of this asymmetric distribution of potential to the damping feature of a surface acoustic wave (SAW), and spin-polarized dependent charge distribution, which

follows $E \propto J_s \times \sigma_s$ [26], where J_s is the flow direction of spin current and σ_s is the spin polarization. The amplitude of SAW decreases along the propagating direction while the SAW damping in the transverse direction is negligible, resulting in a decrease of generated spin current density only in the propagation direction. The decrease in spin current density induces different potential contribution of the transverse component for the electrodes located at the beginning and the end of the wire under test, with respect of SAW wavevector k , as schematically shown in 2.6, which is reflected as an additional asymmetry on the longitudinal signal as shown in 2.6(a, b). Due to this anisotropic distribution, the conventional analysis model for one-dimension charge potential distribution cannot be applied to our experiment. By taking the asymmetric transverse component contribution into account, we adopted the following expression:

$$V_L(\theta)/R = [\mu_0 h_{rf}]^2 (C_T \sin(\theta) + C_L \cos(\theta)) \quad (2.13)$$

Where C_T refers to the conversion factor of transverse contribution and C_L to the longitudinal contribution. Note that C_T and C_L are constants, proportional to C_1 in equation 2.8 independent of θ . As the transverse contribution and longitudinal contribution have different angular dependence, we can separate the transverse and longitudinal contribution by fitting our data with equation 2.13. To test our hypothesis of the asymmetric potential distribution, we measured the two different configurations of electrodes (as depicted in figure 2.6 (a, b)). The measurements are carried out in a different set of samples to those used in the section 1.4 to verify reproducibility for completeness. In the data plotted in figure 2.6(c, d), we observed the reversal of the asymmetry of the potential distribution in the angular variation of longitudinal voltage. This observation agrees well with the magnetic field dependent anisotropic distribution of charge potential, shown in figure 2.6(c, d). In order to map out accurately the total area of our sample, a laborious analysis of potential has to be done with several combinations of electrodes positions, which is beyond the present study.

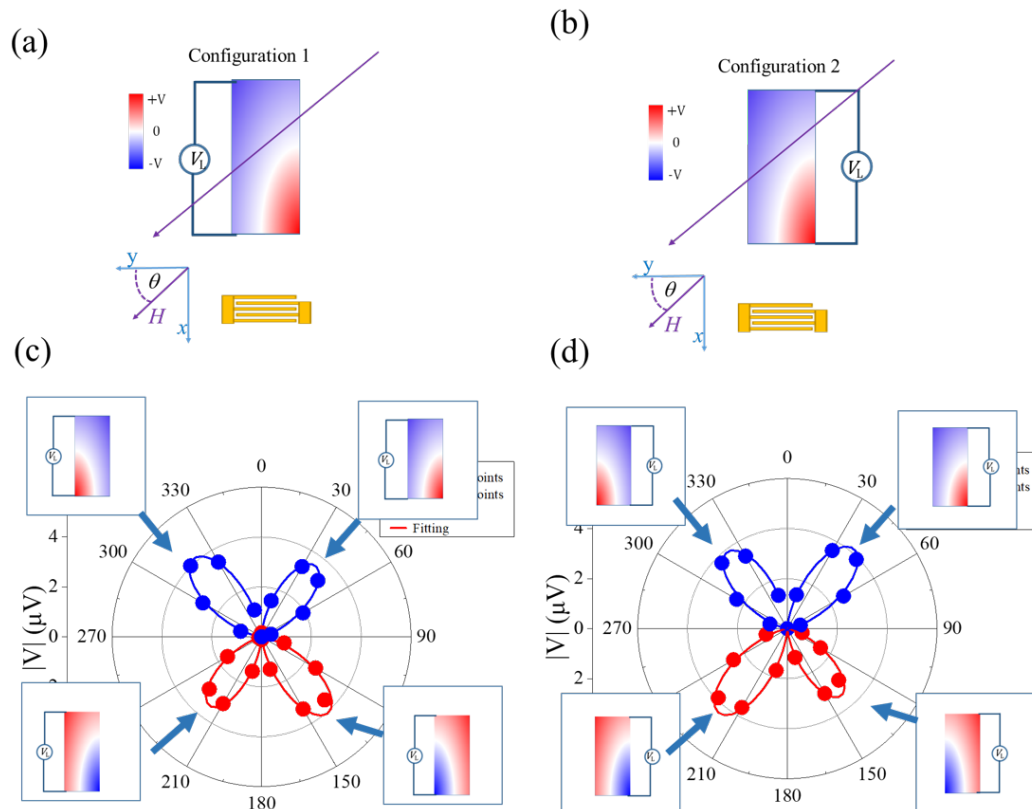


Fig. 2.6 (a, b) Schematic of measurement configuration 1 and configuration 2, and anisotropic distribution of charge potential; (c, d) Angular variation of transverse voltage measured with configuration 1 and configuration 2.

2.4 Conclusions and outlook

We demonstrate the spin to charge current conversion via magnon-phonon coupling and inverse Edelstein effect at the hybrid device Ni/Cu(Ag)/Bi₂O₃. The generation of spin current ($J_s \approx 10^8 A/m^2$) due to magnon - phonon coupling reveals the viability of acoustic spin pumping as a mechanism for the development of Spintronics devices. Full in-plane magnetic field angle dependence of power absorption and the combination of longitudinal and transverse voltage detection reveals symmetric and asymmetric components of acoustic spin pumping voltage induced by Rayleigh-type surface acoustic waves. While the symmetric components are well studied, asymmetric components are widely unexplored. We assign the asymmetric contributions to the interference between longitudinal and shear waves and anisotropic charge distribution at our hybrid devices.

Chapter 3

Conclusions and future perspectives

3.1 Conclusions

In this thesis, we demonstrate the spin to charge current conversion via magnon-phonon coupling and inverse Edelstein effect at the hybrid devices Ni/Cu(Ag)/Bi₂O₃. The generation of spin current ($J_s \approx 1.6 \times 10^8 A/m^2$) due to magnon-phonon coupling proves the feasibility of acoustic spin pumping as a mechanism for the development of Spintronics devices.

The opposite sign in measured signals reflects the opposite spin-momentum locking configuration at Cu/Bi₂O₃ and Ag/Bi₂O₃ interfaces, agrees well with the experiment by standard spin pumping method [23] and optical characterization by magneto-optical Kerr effect which justifies the reliability of the present work.

We observed three different asymmetries in measurement. We assign the asymmetry in power absorption and transverse voltage to the interference between longitudinal and shear waves and asymmetry in longitudinal voltage detection to the anisotropic charge distribution at our hybrid device.

The success of present work reveals the potential of acoustic spin pumping method as the spin current generator, gives new insights toward selectively controlling different types of acoustic phonons by Spintronics devices, advancing the understanding of spin conversion phenomena.

3.2 Future perspectives

The magnetoelastic effect induced magnon-phonon is not the only approach to correlated mechanical oscillations with spins. Since the discovery of the Barnett effect, there is a continuous interest in research towards revealing the mysterious relation between mechanical angular momentum and spin. The reciprocal effect of Barnett effect was later established by Einstein and de Haas, well known as Einstein the only experiment.

Barnett effect describes the magnetization of a matter induced by a spinning motion of itself while Einstein-de Haas effect explains the spinning motion induced by the magnetization of a suspended matter. These two effects give us the most initial idea of the relationship between mechanical angular momentum and spin, which changed the general view of magnetism fundamentally.

The basic concept behind these two is rather simple, which is the angular momentum conservation rule from a quantum mechanics perspective. The externally added mechanical angular momentum induced an unbalanced state, forces the system to align the spin state of the electron to compensate themselves, which realized as Barnett effect. Moreover, in the Einstein-de Haas effect, the magnetization process induced additional angular momentum macro metrically relaxes as the spinning motion of the matter.

In this section, we introduce the basic concept of spin rotation coupling, a variation of the Barnett effect, followed by numerical simulation results.

3.2.1 Spin rotation coupling via surface acoustic waves

Recently, Matsuo et al., published a theoretical framework for the generation of pure spin current by elastic mechanical rotation (spin-rotation coupling, SRC), as a variation of Barnett effect in non-magnetic materials. When waves couple with nonmagnetic materials, the torsion field induced by surface acoustic waves (SAWs) gives the Coriolis force to electrons, rearrange the spin states, inducing non-equilibrium spin accumulation. Along the out of plane axis, the damping of waves gives a gradient of spin accumulation, in analogy to Stern-Gerlach effect, resulting in spin current flowing perpendicularly. However, the torsion field changes its direction every half acoustic wavelength. As a result, the spin current has an AC feature, adding difficulties for the typical transport measurements. Also, the piezoelectricity and continuous periodic deformation accompanying waves may bring tremendous types of spurious signals. In order to overcome these issues,

we propose optical characterization using magneto-optical Kerr effect (MOKE) as an unambiguous detection method to demonstrate the direct coupling between mechanical angular momentum and spin (see figure 3.1).

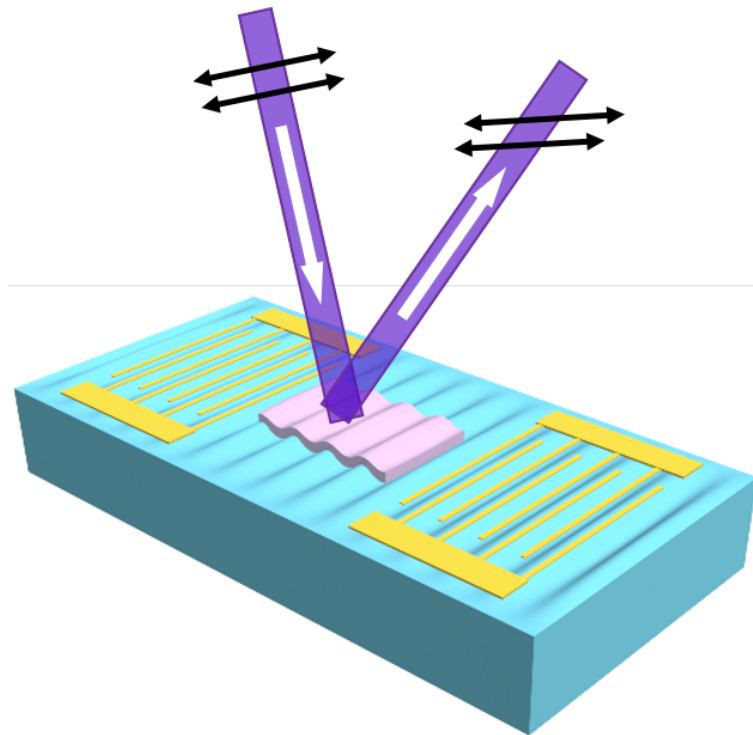


Fig. 3.1 Schematics of optical characterization on spin rotation coupling

bbb

3.2.2 Numerical simulation results

In order to obtain preliminary information, we start with a numerical simulation using COMSOL-Multiphysics (see figure 3.2, quantifying the magnitude of the spin current generated via SRC. Up to now, we have completed the numerical simulation of SRC with SAWs which resonate at 2.5GHz in Cu, Al, Ag, and GaAs. According to the simulation result, among the candidates, Cu performs best regarding generation of spin current, $J_s = 1.10 \times 10^7 A/m^2$.

The next target of numerical simulation focus on revealing the relation between SAWs frequency and the quantity of spin current originated by SRC. According to the theoretical prediction, spin current increases dramatically with respect to frequency, indicating that ultra-high efficient generation of spin current can be

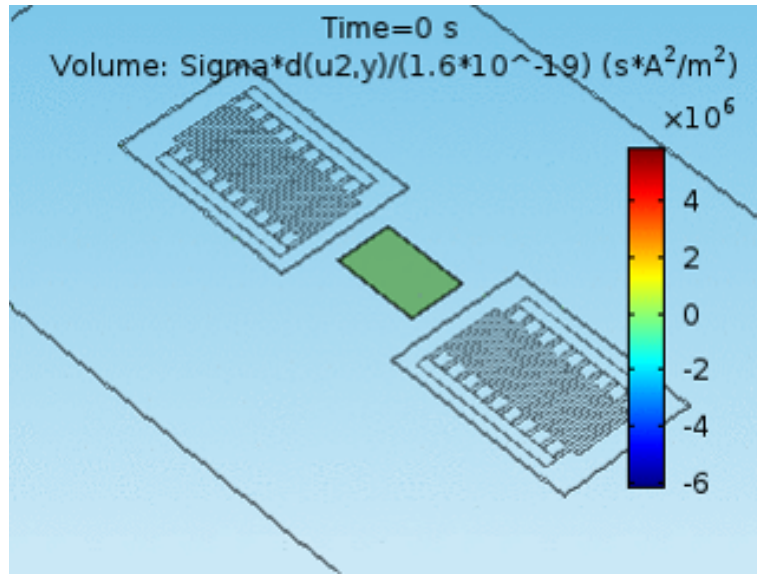


Fig. 3.2 Screenshot of simulation model in COMSOL-Multiphysics

possibly achieved in the high-frequency region. Besides, the frequency dependence of spin current can be used as the proof to justify the origin of the signal.

Table 3.1 Numerical simulation results

Materials	J_s (in 2.5GHz)
Pt	$1.77 \times 10^4 \text{ A/m}^2$
Cu	$1.10 \times 10^7 \text{ A/m}^2$
Ag	$6.86 \times 10^5 \text{ A/m}^2$
Au	$6.10 \times 10^5 \text{ A/m}^2$
GaAs	885 A/m^2

3.2.3 Expected outcome

The present research proposal aims at the novel generation of spin current by surface acoustic waves. This method is based on the spin rotation coupling and does not require strong spin-orbit interaction, opposing to the generation of spin current by known methods, such as Spin Hall effect. As far as my knowledge concerns at this point, there is no direct experimental evidence of spin current generation by mechanical oscillation in the absence of magnetic material, which is an essential building block for the development of energy efficient "Spintronic devices" free of ferromagnetic materials and spin-orbit interaction.

The overall purpose of our research project is to settle a better understanding of the mechanical angular momentum to spin conversion phenomena, through experimental evidence and systematic studies. The success of this project will bring a fundamentally new method of generation of spin current, advancing the understanding of spin conversion phenomena, and gives new insight towards future electronic devices.

References

- [1] YoshiChika Otani, Masashi Shiraishi, Akira Oiwa, Eiji Saitoh, and Shuichi Murakami. Spin conversion on the nanoscale. *Nature Physics*, 13:829, 2017.
- [2] Mingran Xu, Jorge Puebla, Florent Auvray, Bivas Rana, Kouta Kondou, and Yoshichika Otani. Inverse edelstein effect induced by magnon-phonon coupling. *Physical Review B*, 97(18):180301, 2018. PRB.
- [3] Jorge Puebla, Florent Auvray, Mingran Xu, Bivas Rana, Antoine Albouy, Hanshen Tsai, Kouta Kondou, Gen Tatara, and Yoshichika Otani. Direct optical observation of spin accumulation at nonmagnetic metal/oxide interface. *Appl. Phys. Lett.*, 111(9):092402, 2017.
- [4] Florent Auvray, Jorge Puebla, Mingran Xu, Bivas Rana, Daisuke Hashizume, and Yoshichika Otani. Spin accumulation at nonmagnetic interface induced by direct rashba–edelstein effect. *Journal of Materials Science: Materials in Electronics*, 2018.
- [5] M. Weiler, L. Dreher, C. Heeg, H. Huebl, R. Gross, M. S. Brandt, and S. T. B. Goennenwein. Elastically driven ferromagnetic resonance in nickel thin films. *Phys. Rev. Lett.*, 106(11):117601, 2011. PRL.
- [6] L. Dreher, M. Weiler, M. Pernpeintner, H. Huebl, R. Gross, M. S. Brandt, and S. T. B. Goennenwein. Surface acoustic wave driven ferromagnetic resonance in nickel thin films: theory and experiment. *Phys. Rev. B*, 86(13):134415, 2012. PRB.
- [7] R. Sasaki, Y. Nii, Y. Iguchi, and Y. Onose. Nonreciprocal propagation of surface acoustic wave in ni/linbo₃. *Physical Review B*, 95(2):020407, 2017. PRB.
- [8] Zinoviy Nazarchuk, Valentyn Skalskyi, and Oleh Serhiyenko. *Acoustic Emission: Methodology and Application*. Springer, 2017.
- [9] Shutaro Karube, Kouta Kondou, and YoshiChika Otani. Experimental observation of spin-to-charge current conversion at non-magnetic metal/bi₂o₃ interfaces. *Applied Physics Express*, 9(3), 2016.
- [10] Junyeon Kim, Yan-Ting Chen, Shutaro Karube, Saburo Takahashi, Kouta Kondou, Gen Tatara, and YoshiChika Otani. Evaluation of bulk-interface contributions to edelstein magnetoresistance at metal/oxide interfaces. *Physical Review B*, 96(14):140409, 2017. PRB.

- [11] MI D'yakonov and VI Perel. Possibility of orienting electron spins with current. *Soviet Journal of Experimental and Theoretical Physics Letters*, 13:467, 1971.
- [12] AA Bakun, BP Zakharchenya, AA Rogachev, MN Tkachuk, and VG Fleisher. Observation of a surface photocurrent caused by optical orientation of electrons in a semiconductor. *JETP Lett*, 40(11), 1984.
- [13] J. C. Rojas Sánchez, L. Vila, G. Desfonds, S. Gambarelli, J. P. Attané, J. M. De Teresa, C. Magén, and A. Fert. Spin-to-charge conversion using rashba coupling at the interface between non-magnetic materials. *Nature Communications*, 4:2944, 2013.
- [14] Yu A Bychkov and EI Rashba. Properties of a 2d electron gas with lifted spectral degeneracy. *JETP lett*, 39(2):78, 1984.
- [15] Hendrik Bentmann, Takuya Kuzumaki, Gustav Bihlmayer, Stefan Blügel, Eugene V. Chulkov, Friedrich Reinert, and Kazuyuki Sakamoto. Spin orientation and sign of the rashba splitting in bi/cu(111). *Physical Review B*, 84(11):115426, 2011.
- [16] L. Petersen and P. Hedegård. A simple tight-binding model of spin-orbit splitting of sp-derived surface states. *Surface Science*, 459(1):49–56, 2000.
- [17] R. Romestain, S. Geschwind, and G. E. Devlin. Measurement of the linear k term in a polar crystal (cds) by spin-flip raman scattering. *Physical Review Letters*, 39(24):1583–1586, 1977.
- [18] J. Luo, H. Munekata, F. F. Fang, and P. J. Stiles. Observation of the zero-field spin splitting of the ground electron subband in gasb-inas-gasb quantum wells. *Phys. Rev. B*, 38:10142–10145, Nov 1988.
- [19] G. Bihlmayer, S. Blügel, and E. V. Chulkov. Enhanced rashba spin-orbit splitting in BiAg(111) and PbAg(111) surface alloys from first principles. *Physical Review B*, 75(19):195414, 2007.
- [20] Isabella Gierz, Benjamin Stadtmüller, Johannes Vuorinen, Matti Lindroos, Fabian Meier, J. Hugo Dil, Klaus Kern, and Christian R. Ast. Structural influence on the rashba-type spin splitting in surface alloys. *Physical Review B*, 81(24):245430, 2010.
- [21] V. M. Edelstein. Spin polarization of conduction electrons induced by electric current in two-dimensional asymmetric electron systems. *Solid State Communications*, 73(3):233–235, 1990.
- [22] Ka Shen, G. Vignale, and R. Raimondi. Microscopic theory of the inverse edelstein effect. *Physical Review Letters*, 112(9):096601, 2014.
- [23] Hanshen Tsai, Shutaro Karube, Kouta Kondou, Naoya Yamaguchi, Fumiyuki Ishii, and Yoshichika Otani. Clear variation of spin splitting by changing electron distribution at non-magnetic metal/bi₂o₃ interfaces. *Scientific Reports*, 8(1):5564, 2018.

- [24] Antonio Azevedo, A. B. Oliveira, F. M. de Aguiar, and S. M. Rezende. Extrinsic contributions to spin-wave damping and renormalization in thin $\text{ni}_{50}\text{fe}_{50}$ films. *Phys. Rev. B*, 62(9):5331–5333, 2000. PRB.
- [25] M. Weiler, H. Huebl, F. S. Goerg, F. D. Czeschka, R. Gross, and S. T. B. Goennenwein. Spin pumping with coherent elastic waves. *Physical Review Letters*, 108(17):176601, 2012. PRL.
- [26] K. Ando, S. Takahashi, J. Ieda, Y. Kajiwara, H. Nakayama, T. Yoshino, K. Harii, Y. Fujikawa, M. Matsuo, S. Maekawa, and E. Saitoh. Inverse spin-hall effect induced by spin pumping in metallic system. *Journal of Applied Physics*, 109(10):103913, 2011.
- [27] Wei Zhang, Matthias B. Jungfleisch, Wanjun Jiang, John E. Pearson, and Axel Hoffmann. Spin pumping and inverse rashba-edelstein effect in nife/ag/bi and nife/ag/sb . *Journal of Applied Physics*, 117(17):17C727, 2015.
- [28] Mahdi Jamali, Joon Sue Lee, Jong Seok Jeong, Farzad Mahfouzi, Yang Lv, Zhengyang Zhao, Branislav K. Nikolić, K. Andre Mkhoyan, Nitin Samarth, and Jian-Ping Wang. Giant spin pumping and inverse spin hall effect in the presence of surface and bulk spin-orbit coupling of topological insulator bi_2se_3 . *Nano Letters*, 15(10):7126–7132, 2015.
- [29] O. Mosendz, V. Vlaminck, J. E. Pearson, F. Y. Fradin, G. E. W. Bauer, S. D. Bader, and A. Hoffmann. Detection and quantification of inverse spin hall effect from spin pumping in permalloy/normal metal bilayers. *Physical Review B*, 82(21):214403, 2010. PRB.

